Proceedings of the Combustion Institute 41 (2025) 105851

Contents lists available at ScienceDirect

Proceedings of the Combustion Institute

journal homepage: www.elsevier.com/locate/proci

Structure and nitrogen oxide emissions of confined turbulent hydrogen jet flames

T.L. Howarth [a,*], S. Nerzak [a], P. Gruhlke [b], J.T. Lipkowicz [b], L. Panek [b], S. Pfadler [b], M. Gauding [a], H. Pitsch [a]

[a] Institute for Combustion Technology, RWTH Aachen University, 52056 Aachen, Germany
[b] Siemens Energy Global GmbH & Co. KG., Rheinstraße 100, 45478 Mülheim an der Ruhr, Germany

ARTICLE INFO

Dataset link: https://doi.org/10.18154/RWTH-2025-07748

Keywords:
Hydrogen
Differential diffusion
Confined jet
Nitrogen oxide emissions

ABSTRACT

In this work, a database analysis of three-dimensional direct numerical simulations using detailed chemistry is presented considering a turbulent lean premixed hydrogen/air round jet flame at elevated pressure and temperature ($\phi = 0.5, T_u = 530\text{K}, p = 8\text{atm}$), subject to different levels of domain confinement by solid walls. It is shown that for sufficiently small domain sizes, a coherent recirculation zone is present as expected; however, this does not affect the flame structure, consistent with experiments of attached hydrogen flames. Examination of velocity statistics indicates that, while both turbulent kinetic energy and Reynolds shear stresses increase with increasing domain size, these changes occur sufficiently far away from the flame. Each of the flames experiences the same level of mean shear, leading to the same flame structure. Despite identical turbulence-flame interactions between cases, nitrogen oxide (NO) emissions from the flames are observed to be different. For flames with recirculation zones comparable in size to the flame height, the superadiabatic temperatures caused by intrinsic flame instability are retained within the recirculation zone. Often, residence times in the post-flame are too short for locally elevated temperatures to have a significant impact on thermal NO formation. However, when these higher temperatures are coupled with the long fluid residence time in the recirculation zone, despite lower global residence times, this analysis shows that NO emissions from the flame can be enhanced.

1. Introduction

With the ongoing transition to net zero carbon emissions, the usage of hydrogen for power and propulsion systems is becoming an attractive option due to its carbon-free nature and high potential combustion efficiency [1]. In particular, burning hydrogen in a lean, premixed mode can mitigate the potential for nitrogen oxide (NO) emissions, which need to be avoided in such systems. However, in this configuration flames can be subject to strong differential diffusion effects, leading to thermodiffusive instability. Such instability is further enhanced by turbulence [2–4] and persists at high pressures and temperatures typically employed in industrial systems [5–7]. Characteristic markers of thermodiffusive instability include enhanced local reactivity, cellular structures and superadiabatic temperatures [8]. In a turbulent jet configuration, thermodiffusive instability leads to considerably shorter flames than expected, due to the high turbulent burning velocity resulting from enhanced local reactivity [3].

In a confined configuration, whether that be due to walls or the presence of adjacent injectors, the pressure drop through the inflow leads to the formation of recirculation regions. Depending on the geometry, structure of the flow and jet velocities, the fluid residence time in such recirculation regions can be very long. It would be expected that in the presence of recirculation regions, mean shear would be increased compared to the presence of a coflow due to flow reversal. However, in a previous experimental study [9], it was noted that for attached hydrogen flames, the structure of the flame was largely unaffected by the presence of recirculation. The behaviour was attributed to the preheating of the system and high reactivity of hydrogen, but not explained in detail.

NO emissions in lean premixed hydrogen flames have been considered before [10,11], with additional production found to be due to the consumption of nitrogen through the NNH pathway, and is associated with the effect of differential diffusion. Despite the presence of local superadiabatic temperatures, the production of thermal NO is largely unaffected due to both low temperatures and short residence time in the post-flame. However, these studies only considered configurations where the flow is allowed to escape the post-flame region rapidly,

* Corresponding author.
E-mail address: t.howarth@itv.rwth-aachen.de (T.L. Howarth).

https://doi.org/10.1016/j.proci.2025.105851
Received 22 April 2025; Accepted 4 September 2025
Available online 19 September 2025

i.e. unconfined, statistically planar flames. In other configurations, such as a confined jet, the geometry dictates the residence time of the flow, and the production of thermal NO could be affected.

This work aims to determine why short, attached hydrogen flames may be largely unaffected by the presence of recirculation, and whether the wide range of fluid timescales, combined with superadiabatic temperatures arising from thermodiffusive instability, can affect NO formation and emissions of the flame. In Section 2, the numerical solver, simulation configuration and different averaging procedures are discussed. Then, the structure of the flame and confined flow are analysed in Section 3.1, before examining the NO emissions of the flame in Section 3.2.

2. Direct numerical simulation database

In this section, the solver, database and different methods used for averaging are briefly discussed.

2.1. Numerical solver

Three-dimensional direct numerical simulations are performed using PeleLMeX. PeleLMeX solves the reacting Navier–Stokes equations in the low-Mach number limit, where the fluid is treated as a mixture of ideal gases. A mixture-averaged model is used to determine species diffusion coefficients, and the Soret effect is included as presented in [12]. The discretisation is based on a second-order Godunov (finite-volume) formulation, where the advection, diffusion and reactive terms are coupled together through a spectral deferred correction approach [13]. A density-weighted projection method is used to enforce the divergence constraint [14], which also incorporates the equation of state [15]. The discretisation is integrated with timesteps determined by the advective CFL number, where diffusion and reaction are treated implicitly. The scheme is embedded into a block-structured adaptive mesh refinement framework provided by AMReX [16]. Further details can be found in [17]. Transport coefficients, thermodynamic relationships and chemical kinetics were taken from a detailed chemical mechanism containing 18 species and 106 reactions [18]. In addition to the momentum, species and energy equations, the solver has been supplemented with a fluid age equation, given by

$$\frac{\partial \rho \mathcal{A}}{\partial t} + \nabla \cdot (\rho \mathbf{u} \mathcal{A}) = \nabla \cdot (D \nabla \mathcal{A}) + \rho, \tag{1}$$

where $\mathcal{A}$ is the fluid age [19], ρ is the density and D is a diffusion coefficient. For this work, D was chosen to be equal to the dynamic viscosity of the fluid.

2.2. Simulation configuration

The simulation was set up with a round jet of diameter $d = 1\,\text{mm}$ on the low z boundary, with the rest of the boundary set to an isothermal no-slip wall at $T_{\text{wall}} = T_{\text{ad}}$. The lateral x and y boundaries are set as adiabatic no-slip walls, and the z high boundary is set as an outflow. The usage of adiabatic walls naturally affects the production of NO, with the present study designed to isolate the effects of the flame and flow, rather than the impact of boundary conditions. A precursor simulation was run of a turbulent periodic pipe flow at a Reynolds number of 10 000 to generate a turbulent inflow. This was computed using the embedded boundaries feature provided by AMReX to implicitly represent the round geometry. Mean profiles of the streamwise velocity for the inflow are provided as supplementary material. Slices are then sampled from this precursor simulation and used as an evolving inflow condition to the reacting simulation. To fully establish the recirculation zones, the simulation is firstly run at the coarse resolution ($\Delta x_0 = 20$ μm) for 20 bulk flow-through times, which also establishes the steadiness of the fluid age variable. Adaptive mesh refinement is then turned on, with the first level covering the cold portion of the jet by tagging cells with a temperature less than 700 K and the second level covering the flame by tagging based on the intermediate species HO_2. This strategy allows for flow establishment at a reasonable computational cost, before collecting statistics from high-resolution data with accurate local flame speeds and chemistry in the statistically steady region. Three cases are considered with varying domain widths and are referred to throughout as cases L2, L3 and L4. The parameters for each simulation are listed in Table 1; note the different domain widths used in each case. The value of the instability parameter ω_2 is calculated following [6], and the freely-propagating (FP) thickness l_F and speed s_F are calculated following the model from [4]. Here, a freely-propagating flame is taken to be a planar, laminar flame, potentially under the influence of intrinsic flame instabilities.

Table 1
Simulation parameters.

Property	Value
Equivalence ratio, ϕ	0.5
Unburnt temperature (K)	530
Pressure (atm)	8.0
Adiabatic flame temperature T_{ad} (K)	1830
Second-order instability parameter ω_2	2.85
Unstretched flame thickness, l_L (μm)	48
Unstretched flame speed, s_L (m s^{-1})	0.979
FP flame speed s_F (m s^{-1})	1.23
FP flame thickness l_F (μm)	40
Jet velocity u_j (m s^{-1})	63
Jet Reynolds number, Re_j	10 000
Jet diameter d (mm)	1
Jet area A_j (m^2)	7.85×10^{-7}
Kolmogorov length scale η_{min} (μm)	6.8
Domain length L_z (mm)	16
Domain widths $L_{x,y}$ (mm)	L2: 2 L3: 3 L4: 4
Coarse resolution Δx_0 (μm)	20.8
Fine resolution Δx_2 (μm)	5.2

2.3. Averaging procedures

Several different averages are used throughout this work. First, ensemble averaging of a quantity ϕ is given by

$$\langle \phi \rangle_t = \frac{1}{N} \sum_{t=t_1}^{t_N} \phi(\mathbf{x}, t). \tag{2}$$

Then, a surface-conditioned, ensemble average is given by

$$\langle \phi \rangle_s^{C=C_0} = \left\langle \frac{1}{A_T} \int_{\Gamma(C=C_0)} \phi \, d\Gamma \right\rangle_t \tag{3}$$

on isosurface $\Gamma(C = C_0)$ for a given scalar C, where the surface area A_T and reference area A_0 are given by

$$A_T^{C=C_0} = \int_{\Gamma(C=C_0)} d\Gamma, \; A_0^{C=C_0} = \int_{\Gamma(\langle C \rangle_t = C_0)} d\Gamma. \tag{4}$$

The conditioning of this average on the streamwise distance is denoted by $\langle \phi \rangle_{s|z}^{C=C_0}$. An azimuthal average is constructed as

$$\overline{\phi} = \begin{cases} \dfrac{1}{2\pi} \displaystyle\int_0^{2\pi} \langle \phi \rangle_t \, d\theta, \text{ for } r < \frac{L_x}{2} \\ \displaystyle\sum_{n=0}^{3} \frac{1}{\beta_n - \alpha_n} \int_{\alpha_n}^{\beta_n} \langle \phi \rangle_t \, d\theta, \text{ otherwise} \end{cases} \tag{5}$$

for azimuthal and radial coordinates $\theta = \arctan(y/x)$, $r = \sqrt{x^2 + y^2}$ respectively. The integral bounds are given by

$$\alpha_n = \frac{n\pi}{2} + \cos^{-1}\left(\frac{L_x}{2r}\right), \quad \beta_n = \frac{(n+1)\pi}{2} - \cos^{-1}\left(\frac{L_x}{2r}\right). \tag{6}$$

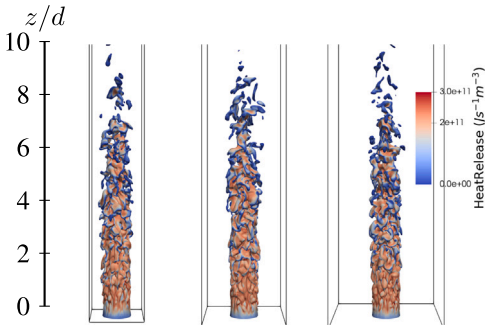

Fig. 1. Isosurfaces of cases L2, L3 and L4 coloured by local heat release; the black box outline indicates the domain. (For interpretation of the references to colour in this figure legend, the reader is referred to the web version of this article.)

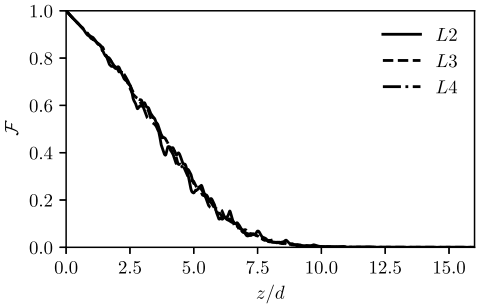

Fig. 2. Fuel flux $\mathcal{F}$ as a function of streamwise distance.

The second case in Eq. (5) arises from taking an azimuthal average in a non-cylindrical domain to weight the corners appropriately. The corresponding Favre-average is given by $\widetilde{\phi} = \overline{\rho\phi}/\overline{\rho}$. Finally, a standard planar average is given by

$$\langle\phi\rangle = \frac{1}{L_x L_y}\int_0^{L_y}\int_0^{L_x}\langle\phi\rangle_t \, dx \, dy \tag{7}$$

with corresponding Favre average $\langle\phi\rangle_F = \langle\rho\phi\rangle/\langle\rho\rangle$.

3. Results

In this section, the instantaneous and mean velocity and scalar statistics are analysed to determine the effect of confinement on the flame, flow and emission characteristics.

3.1. Flame structure

Isosurfaces throughout this work are constructed using the fuel-based progress variable, given by

$$c_{\mathrm{H_2}} = 1 - \frac{Y_{\mathrm{H_2}}}{Y_{\mathrm{H_2,u}}}, \tag{8}$$

where $Y_{\mathrm{H_2}}$ is the mass fraction of hydrogen, and the u subscript denotes unburnt quantities. Instantaneous isosurfaces of each flame are shown in Fig. 1, taken at the $c_{\mathrm{H_2}} = 0.9$ isosurface, and coloured by local heat release. It can be immediately seen that the flames appear to be nearly identical. To identify the flame length, Fig. 2 shows the normalised fuel flux $\mathcal{F}$, defined as

$$\mathcal{F} = \frac{L_x L_y}{\rho_u Y_{\mathrm{H_2},u} u_j A_j}\langle\rho Y_{\mathrm{H_2}} u_z\rangle. \tag{9}$$

At $z = 7.5d$, $\mathcal{F} \approx 0.02$ for all cases, indicating that the flame length is approximately $7.5d$, and analysis from here on is restricted to $z < 7.5d$.

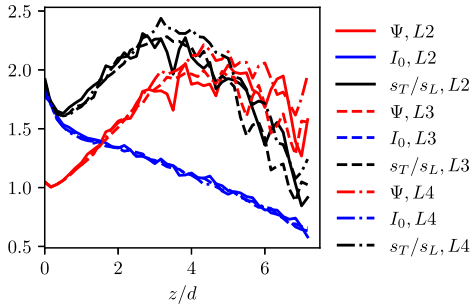

Fig. 3. Flame surface wrinkling Ψ, normalised local reactivity I_0 and normalised turbulent flame speed s_T/s_L as a function of streamwise distance.

Fig. 3 shows the flame wrinkling Ψ, normalised local reactivity I_0 and normalised turbulent flame speed s_T/s_L given by

$$\Psi = \frac{A_T^{c_{\mathrm{H_2}}=0.9}(z)}{A_0^{c_{\mathrm{H_2}}=0.9}(z)} \tag{10}$$

$$I_0 = \frac{L_x L_y}{\rho_u Y_{\mathrm{H_2},u} A_T(z)}\langle\dot{\omega}_{\mathrm{H_2}}\rangle, \tag{11}$$

$$s_T/s_L = I_0\Psi. \tag{12}$$

These quantities are identical in all three cases; however, the trends are notably different from those found in hydrogen slot jets. In the slot jet, I_0 has a spatially uniform value from just after the nozzle until just short of the flame tip [3]. Here, however, I_0 monotonically decreases from around 2 to a less than 1 near the flame tip. To understand this trend, Fig. 4 shows the Karlovitz number Ka, calculated as

$$Ka(z) = \sqrt{\frac{\langle\varepsilon\rangle_{s|z}^{c_{\mathrm{H_2}}=0.1}}{\varepsilon_F}}, \quad \varepsilon = \tau_{ij}''\frac{\partial u_i''}{\partial x_j}, \tag{13}$$

where the surface average has been performed at the $c_{\mathrm{H_2}} = 0.1$ isosurface to obtain statistics close to the flame on the unburnt side. Note that this is different to previous procedures used in other studies of turbulent hydrogen jets (e.g. [3]), so that the turbulence is only characterised by quantities sampled on the unburnt side of the flame. This allows for direct comparison with models developed based on planar flames propagating into homogeneous isotropic turbulence (HIT) [4]. Ka decreases rapidly in the streamwise direction from 70 to less than 5 near the flame tip. Previous work has investigated the effect of Karlovitz number on I_0 [4,20,21], and found that they are positively correlated. Specifically, in HIT, $I_0/I_0^{lam} - 1 \sim \sqrt{Ka}$. To see if this relationship still holds in the jet, Fig. 5 shows Ka against $I_0/I_0^{lam} - 1$ (here $I_0^{lam} \approx 1.2$) on a log–log plot. While a positive correlation is apparent, the $\sqrt{Ka}$ scaling does not appear to hold, with a faster decay than expected in the developed turbulent region ($z/d > 1.5$). A possible reason for this is the negative mean curvature of the jet. To test this hypothesis, another line is plotted weighted by the Markstein model provided in [4], where the mean curvature is taken to be inverse mean radius of the jet. As can be seen, this recovers the profile observed in the developed turbulence region, before significant flame-flame interaction at the flame tip.

Fig. 6 shows $\overline{T}$ for all three cases, with the mean velocity streamlines superimposed. In case L2, the recirculation zones are approximately the same length as the flame ($L_{RZ} = 5d$), and increase to $L_{RZ} = 13d$ for case L4. Another feature is higher average temperatures in the recirculation regions for case L2 compared to cases L3 or L4. Since the condition considered here is thermodiffusively unstable, superadiabatic temperatures are present along the flame front, which can be seen more clearly in instantaneous slices shown in Fig. 7. In all three cases, streamlines emanate from the side of the jet due to dilatation. However, in case L2, a separating streamline impacts the side wall, creating a

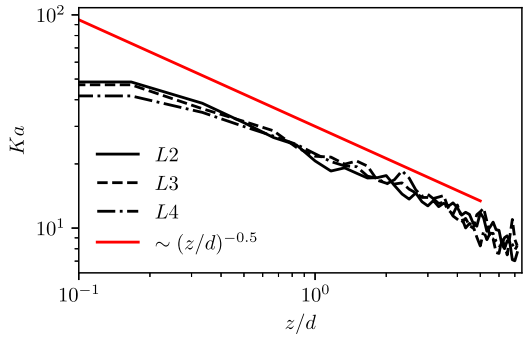

Fig. 4. Karlovitz number Ka as a function of streamwise distance.

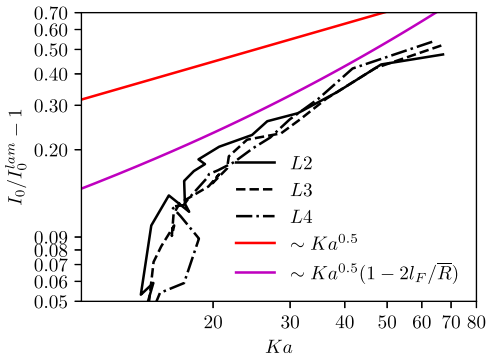

Fig. 5. Rescaled I_0 as a function of Ka; points close to the nozzle are on the right, and points downstream are on the left. The solid red line corresponds to scaling (not the exact model) observed in HIT, and the solid magenta line corrects this scaling based on the mean curvature. (For interpretation of the references to colour in this figure legend, the reader is referred to the web version of this article.)

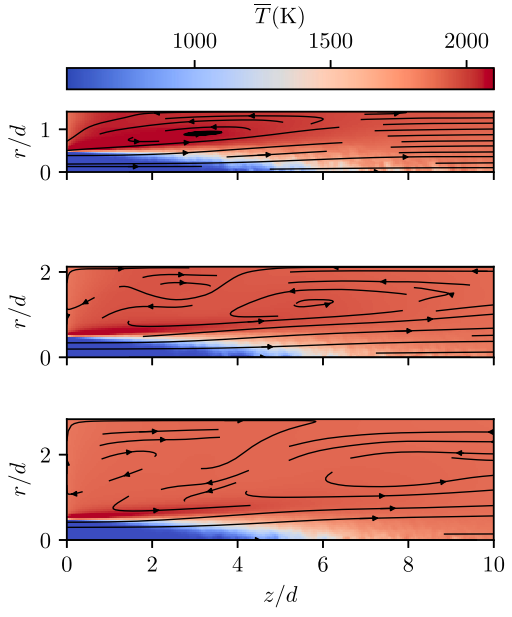

Fig. 6. Average temperature $\overline{T}$ with superimposed velocity streamlines for cases L2 (top), L3 (middle), L4 (bottom).

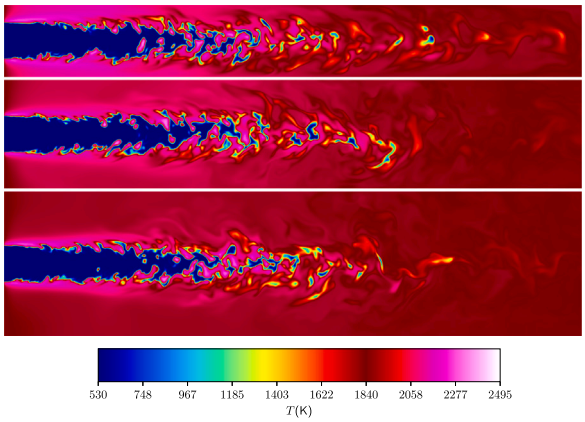

Fig. 7. Slice through $x = 0$ of instantaneous temperature field for case L2 (top), L3 (centre) and L4 (bottom). The red colour corresponds to the adiabatic flame temperature ($T_{ad} = 1840$ K, indicating superadiabatic temperature overshoots around the side of the jet. (For interpretation of the references to colour in this figure legend, the reader is referred to the web version of this article.)

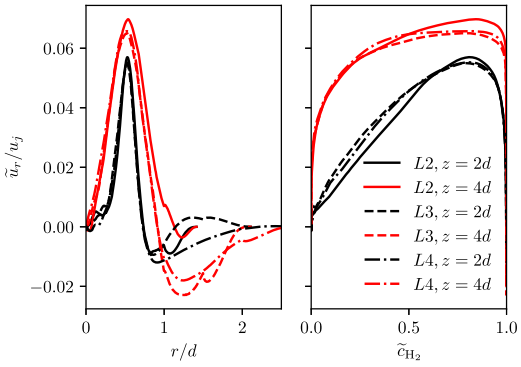

Fig. 8. Normalised Favre-averaged radial velocity $\widetilde{u}_r/u_j$ as functions of normalised radius r/d (left) and $\widetilde{c}_{H_2}$ (right) for positions of $z/d = 2, 4$ for black and red lines respectively. (For interpretation of the references to colour in this figure legend, the reader is referred to the web version of this article.)

closed recirculation volume. Fluid inside this cell is effectively trapped, circulating locally rather than being convected downstream.

Figs. 8 and 9 show the Favre-averaged radial and streamwise velocities as functions of the Favre-averaged fuel-based progress variable c_{H_2} and normalised radius r/d for $z/d = 2$ and $z/d = 4$. Slices through the mean temperature field at these locations are provided as supplementary material. At $z/d = 2$, $\widetilde{u}_r > 0$ across most of the jet for all cases, indicating that there is little to no entrainment through the flame. Note that by using Favre-averaged velocities, rather than Reynolds-averaged, mass fluxes are explicitly examined, rather than volume fluxes as typically done in incompressible jets. If volume fluxes were used instead, the effects of dilatation would need to be considered. Additionally, the streamwise velocity is essentially stagnant outside of the jet, with $\widetilde{u}_z > 0$. This changes further downstream at $z/d = 4$, where for cases L3 and L4, there are significant regions with $\widetilde{u}_r < 0$. However, these are not situated near the flame, with $\widetilde{u}_r > 0$ across the whole range of $\widetilde{c}_{H_2}$ due to thermal expansion. For the streamwise velocity, there are now some regions with $\widetilde{u}_z < 0$, but similar to the radial velocity, it is positive and consistent through the flame for all cases.

Figs. 10 and 11 present the normalised Favre-averaged turbulent kinetic energy (TKE) and Reynolds shear stress (RSS) analogous to Figs. 8 and 9. At $z/d = 2$ there are low levels of both TKE and RSS, with much lower values than seen in typical non-reacting jets [22]. At $z/d = 4$,

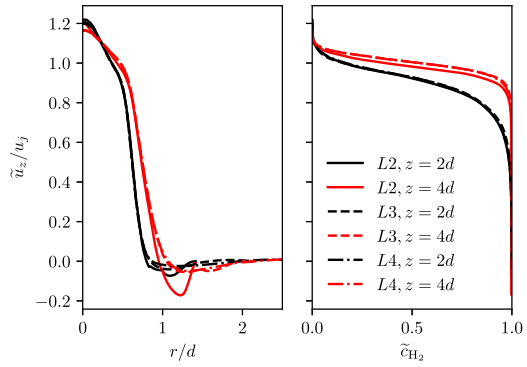

Fig. 9. Normalised Favre-averaged streamwise velocity $\widetilde{u}_z/u_j$ as functions of normalised radius r/d (left) and $\widetilde{c}_{\mathrm{H_2}}$ (right) for positions of $z/d = 2, 4$ for black and red lines respectively. (For interpretation of the references to colour in this figure legend, the reader is referred to the web version of this article.)

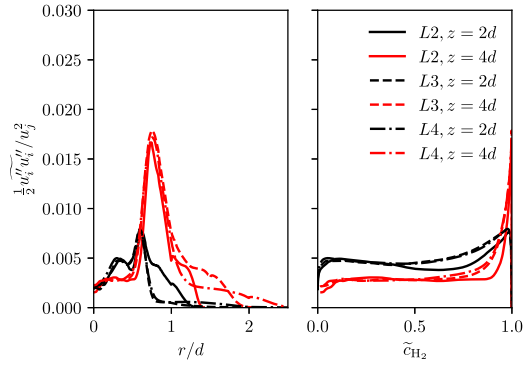

Fig. 10. Normalised Favre-averaged turbulent kinetic energy $\frac{1}{2}\widetilde{u_i''u_i''}/u_j^2$ as functions of normalised radius r/d (left) and $\widetilde{c}_{\mathrm{H_2}}$ (right) for positions of $z/d = 2, 4$ for black and red lines respectively. (For interpretation of the references to colour in this figure legend, the reader is referred to the web version of this article.)

the levels of both quantities have increased and are different for the three cases. As the domain grows, larger eddies can form from the shear layer between the jet and recirculation zone, which inherently break down and increase the Reynolds stresses. However, it can be seen that these differences occur away from the flame. TKE remains essentially constant in the flame between the two positions, while the RSS decreases, indicating a weakening influence of shear on turbulence generation as the flame shifts away from the mean shear layer.

3.2. Nitrogen oxide emissions

Although the flame itself is largely unaffected by the presence of confinement, the mean temperature field is dictated by the presence of recirculation. Since the timescales of the recirculation zone are at least an order of magnitude larger than the jet or bulk flow, high residence times may lead to increased NO emissions through the thermal NO pathway.

Fig. 12 shows $\widetilde{Y}_{\mathrm{NO}}$ for each of the three cases. In case L2, considerably more NO is found in the recirculation regions than in cases L3 or L4. Since the flame structure is identical in each case, the effect of local reactivity fluctuations on NO production through the NNH pathway cannot be expected to change. To demonstrate the difference in residence time in the different cases, Fig. 13 shows the fluid age $\widetilde{\mathcal{A}}$. The fluid residence time in the recirculation zones increases with increasing domain width; this can be simply explained by lower bulk velocities and a larger recirculation bubble. However, in the wider

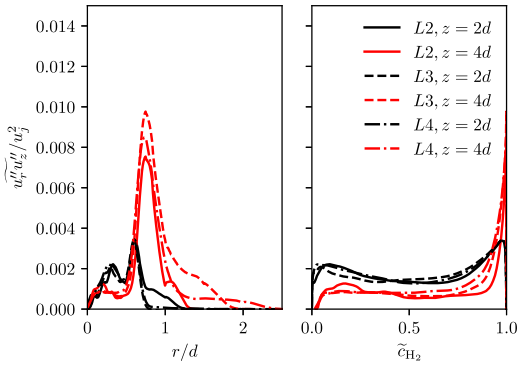

Fig. 11. Normalised Favre-averaged Reynolds shear stress $\widetilde{u_r''u_z''}/u_j^2$ as functions of normalised radius r/d (left) and $\widetilde{c}_{\mathrm{H_2}}$ (right) for positions of $z/d = 2, 4$ for black and red lines respectively. (For interpretation of the references to colour in this figure legend, the reader is referred to the web version of this article.)

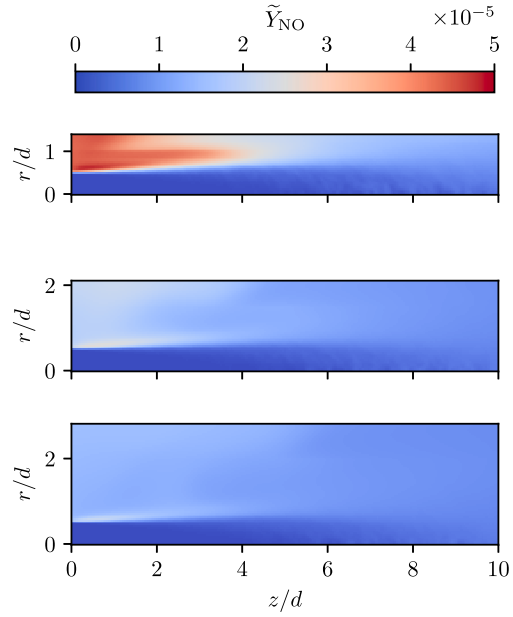

Fig. 12. $\widetilde{Y}_{\mathrm{NO}}$ for the cases L2 (top), L3 (middle) and L4 (bottom).

cases, mean temperatures in the recirculation bubble are lower, and approximately equal to the adiabatic flame temperature (see Fig. 6).

To explain the potentially counterintuitive trend of increasing NO with decreasing global residence times, joint probability distribution functions (JPDFs) between the temperature, fluid age and mass fraction are compared in Fig. 14. It can be seen from the JPDF of T and Y_{NO} that, as expected, Y_{NO} increases exponentially with increasing temperature. Additionally, case L2 exhibits the higher NO mass fractions. This can also be seen as a function of age, where, again, Y_{NO} is positively correlated with $\mathcal{A}$, but with noticeably different gradients across the different cases. This gradient will be closely tied to the temperature, with fluid at higher temperatures not needing to reside for so long to produce NO. The final JPDF between T and $\mathcal{A}$ demonstrates how these regions manifest. In case L2, hot fluid resides for a non-negligible amount of time, leading to a higher conditional mean than seen in the other cases, and producing considerably more NO in these regions, which are found in the recirculation zone.

Fig. 15 shows $\langle Y_{\mathrm{NO}}\rangle_F$ normalised by the exhaust value in case L2 ($\langle Y_{\mathrm{NO}}^{L2}\rangle_F(L_z)$). More NO is found near the inflow as expected and this extra formation leads to an increase in NO at the exhaust, but only 15% more than case L3 and L4. To understand why elevated local values of

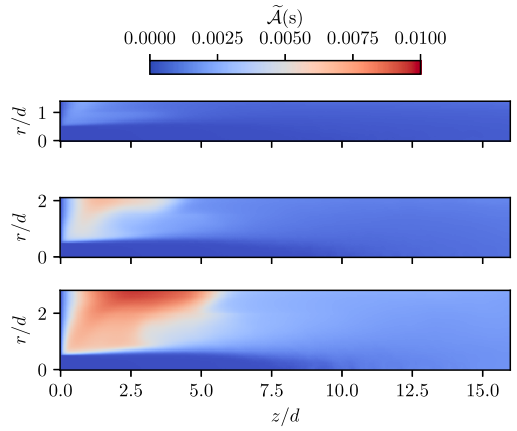

Fig. 13. Favre-averaged fluid age $\widetilde{\mathcal{A}}$ for cases L2 (top), L3 (middle) and L4 (bottom). With increasing domain width, fluid residence time in the recirculation zones increases.

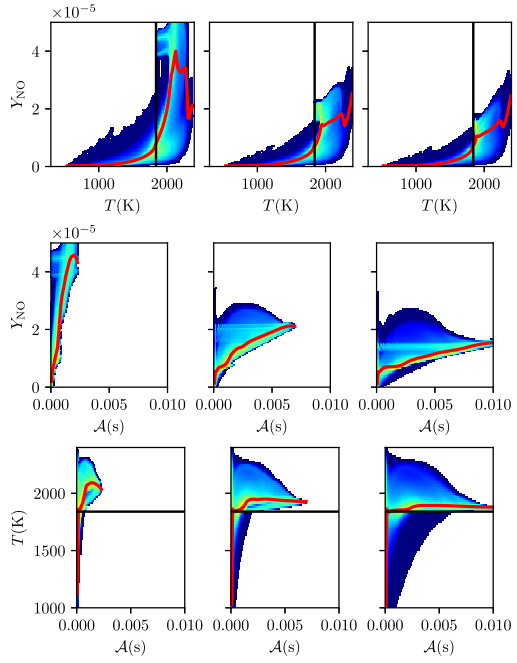

Fig. 14. JPDFs of each combination of temperature T, fluid age $\mathcal{A}$ and Y_{NO} for cases L2 (left), L3 (centre) and L4 (right). Conditional means are given as red lines, and the adiabatic temperature is marked with a black line in the top and bottom figures. (For interpretation of the references to colour in this figure legend, the reader is referred to the web version of this article.)

NO in the recirculation zone are only leading to a small increase in the exhaust value, the mean convective and diffusive fluxes into the jet are computed, defined by

$$C_{NO} = -\overline{\rho u_r Y_{NO}}, D_{NO} = -\overline{\rho D_{NO} \frac{\partial Y_{NO}}{\partial r}}. \quad (14)$$

These quantities, as well as their sum, are evaluated at the $\widetilde{u}_z = 0$ boundary are shown in Fig. 16. The largest fluxes are found for case L2, with this decreasing for cases L3 and L4. The dominant mechanism for transport is lateral convection through entrainment, however, the degree of entrainment has been reduced by heat release compared to a typical jet. This can be seen by evaluating the entrainment coefficient at this boundary, defined as

$$\alpha(z) = -\widetilde{u}_r(r(\widetilde{u}_z = 0), z)/\widetilde{u}_z(0, z) \quad (15)$$

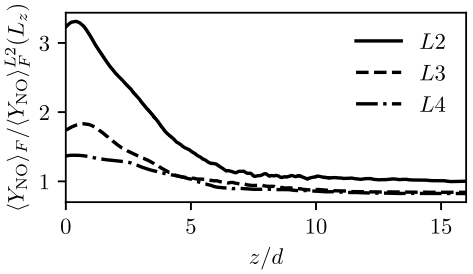

Fig. 15. $\langle Y_{NO}\rangle_F$ as a function of streamwise distance, normalised by the exhaust value for case L2.

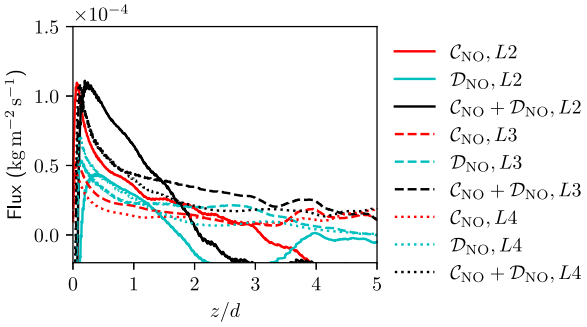

Fig. 16. Convective and diffusive fluxes of NO across the $\widetilde{u}_z = 0$ boundary for each case.

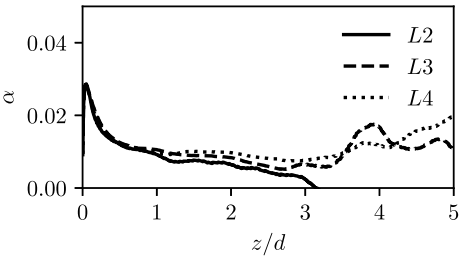

Fig. 17. Entrainment coefficient α as a function of streamwise distance for cases L2,L3 and L4.

which is shown in Fig. 17. The value peaks around 0.03 very near the nozzle before falling quickly to 0.01. This is considerably lower than values seen in incompressible jets, which are typically around 0.05 ∼ 0.07 [23]. Hence, while NO is transported into the jet via both entrainment and diffusion, this is slower than would be in the case in an incompressible jet, leading to a modest increase in NO downstream.

4. Discussion and conclusion

Generation and analysis of a database of direct numerical simulations using finite-rate chemistry of confined hydrogen turbulent jet flames has been carried out to examine the effect of confinement on the structure and NO emissions characteristics.

The structure of the flow is different in each case, with larger recirculation bubbles, and wider domains allowing for the formation of larger turbulent structures. Such structures lead to larger turbulent kinetic energy and Reynolds shear stresses, but sufficiently far away from the flame to not change the flame structure. This results in the same turbulent flame speed, and hence flame length, in all cases. In regions away from the jet exit, the scaling relationship between Ka and I_0 found in HIT ($I_0/I_0^{lam} - 1 \sim \sqrt{Ka}$) is seen not to hold with the data suggesting a faster decay than expected in the developed turbulence region away from the nozzle. The hypothesis for this is that mean

negative curvature of the round jet facilitates this faster-than-expected decay, which is backed up by applying the Markstein model from [4]. Nevertheless, exploring the precise reason for these differences, and comparisons to planar jets which do not experience a negative mean curvature, will be the focus of future work.

Despite the identical structure of the flames, NO emissions from each configuration are different. Interestingly, NO emissions are found to increase with decreasing domain size and residence time, which is opposite to what would typically be anticipated. By comparing the correlations between temperature, fluid age, and NO mass fraction, it was shown that, in the most confined case, superadiabatic temperatures arising from differential diffusion are trapped in the recirculation region, resulting in additional thermal NO production. In the less confined cases, this fluid is expelled rather than recirculated; in a practical system, designs could consider this flushing mechanism to mitigate NO emissions. Due to inhibition of entrainment by heat release, NO is transported slowly into the jet, leading to a modest increase of 15%–20% at the exhaust.

Novelty and significance statement

The novelty of this research is twofold. Firstly, it explains why fast, attached turbulent jet flames are relatively insensitive to the presence of recirculation as observed, but not explained, experimentally. Secondly, this is the first work to demonstrate that combinations of geometry and intrinsic instability can lead to increased NO emissions. It is significant because it demonstrates that mechanisms driving pollutant formation can arise from coupled flamespecific and geometric effects. This highlights the importance of considering flame-flow interactions and intrinsic instabilities in the design of low-emission combustion systems.

CRediT authorship contribution statement

T.L. Howarth: Writing – original draft, Software, Resources, Methodology, Formal analysis, Data curation, Conceptualization. **S. Nerzak:** Writing – review & editing, Conceptualization. **P. Gruhlke:** Writing – review & editing, Project administration, Funding acquisition, Conceptualization. **J.T. Lipkowicz:** Writing – review & editing, Project administration, Funding acquisition, Conceptualization. **L. Panek:** Writing – review & editing, Project administration, Funding acquisition, Conceptualization. **S. Pfadler:** Writing – review & editing, Project administration, Funding acquisition, Conceptualization. **M. Gauding:** Writing – review & editing, Resources, Project administration, Funding acquisition, Conceptualization. **H. Pitsch:** Writing – review & editing, Project administration, Funding acquisition, Conceptualization.

Declaration of competing interest

The authors declare that they have no known competing financial interests or personal relationships that could have appeared to influence the work reported in this paper.

Acknowledgements

TLH acknowledges financial support from Deutsche Forschungsgemeinschaft, Germany (DFG) within the project (ID: 516338899) IRTG 2983 Hy-Potential. SN acknowledges support from the DFG Priority Program SPP 2419 HyCAM. MG and HP acknowledge support from the European Research Council (ERC) Advanced Grant (HYDROGENATE, ID: 101054894). The authors gratefully acknowledge the Gauss Centre for Supercomputing e.V. (www.gauss-centre.eu) for funding this project by providing computing time on the GCS Supercomputers JUWELS at Jülich Supercomputing Centre (JSC) (ID: h2index) and SuperMUC-NG at Leibniz Supercomputing Centre (www.lrz.de) (ID: pn36ga).

Appendix A. Supplementary data

Supplementary material related to this article can be found online at https://doi.org/10.1016/j.proci.2025.105851.

Data availability

The data generated in this study are available on online at https://doi.org/10.18154/RWTH-2025-07748.

References

[1] H. Pitsch, The transition to sustainable combustion: Hydrogen-and carbon-based future fuels and methods for dealing with their challenges, Proc. Combust. Inst. 40 (1–4) (2024) 105638.
[2] A.J. Aspden, M.S. Day, J.B. Bell, Turbulence–flame interactions in lean premixed hydrogen: transition to the distributed burning regime, J. Fluid Mech. 680 (2011) 287–320.
[3] L. Berger, A. Attili, H. Pitsch, Synergistic interactions of thermodiffusive instabilities and turbulence in lean hydrogen flames, Combust. Flame 244 (2022) 112254.
[4] T.L. Howarth, E.F. Hunt, A.J. Aspden, Thermodiffusively-unstable lean premixed hydrogen flames: Phenomenology, empirical modelling, and thermal leading points, Combust. Flame 253 (2023) 112811.
[5] L. Berger, A. Attili, H. Pitsch, Intrinsic instabilities in premixed hydrogen flames: parametric variation of pressure, equivalence ratio, and temperature. Part 2–Non-linear regime and flame speed enhancement, Combust. Flame 240 (2022) 111936.
[6] T.L. Howarth, A.J. Aspden, An empirical characteristic scaling model for freely-propagating lean premixed hydrogen flames, Combust. Flame 237 (2022) 111805.
[7] M. Rieth, A. Gruber, J.H. Chen, The effect of pressure on lean premixed hydrogen-air flames, Combust. Flame 250 (2023) 112514.
[8] L. Berger, K. Kleinheinz, A. Attili, H. Pitsch, Characteristic patterns of thermodiffusively unstable premixed lean hydrogen flames, Proc. Combust. Inst. 37 (2) (2019) 1879–1886.
[9] O. Lammel, M. Stöhr, P. Kutne, C. Dem, W. Meier, M. Aigner, Experimental analysis of confined jet flames by laser measurement techniques, J. Eng. Gas Turbines Power 134 (4) (2012) 041506.
[10] M.S. Day, J.B. Bell, X. Gao, P. Glarborg, Numerical simulation of nitrogen oxide formation in lean premixed turbulent H2/O2/N2 flames, Proc. Combust. Inst. 33 (1) (2011) 1591–1599.
[11] X. Wen, L. Berger, F. Vom Lehn, A. Parente, H. Pitsch, Numerical analysis and flamelet modeling of NOx formation in a thermodiffusively unstable hydrogen flame, Combust. Flame 253 (2023) 112817.
[12] T.L. Howarth, M.S. Day, H. Pitsch, A.J. Aspden, Thermal diffusion, exhaust gas recirculation and blending effects on lean premixed hydrogen flames, Proc. Combust. Inst. 40 (1–4) (2024) 105429.
[13] A. Nonaka, M.S. Day, J.B. Bell, A conservative, thermodynamically consistent numerical approach for low Mach number combustion. Part I: Single-level integration, Combust. Theory Model. 22 (1) (2018) 156–184.
[14] A.S. Almgren, J.B. Bell, P. Colella, L.H. Howell, M.L. Welcome, A conservative adaptive projection method for the variable density incompressible Navier–Stokes equations, J. Comput. Phys. 142 (1) (1998) 1–46.
[15] M.S. Day, J.B. Bell, Numerical simulation of laminar reacting flows with complex chemistry, Combust. Theory Model. 4 (4) (2000) 535.
[16] W. Zhang, A. Almgren, V. Beckner, J. Bell, J. Blaschke, C. Chan, M. Day, B. Friesen, K. Gott, D. Graves, et al., AMReX: a framework for block-structured adaptive mesh refinement, J. Open Source Softw. 4 (37) (2019) 1370.
[17] L. Esclapez, M. Day, J. Bell, A. Felden, C. Gilet, R. Grout, M.H. de Frahan, E. Motheau, A. Nonaka, L. Owen, et al., PeleLMeX: an AMR low mach number reactive flow simulation code without level sub-cycling, J. Open Source Softw. 8 (2023).
[18] Y. Murikami, Q.-D. Wang, S. Liu, P. Wang, L.P. Maffei, R. Langer, T. Faravelli, H. Pitsch, J. Bergthorson, G. Bourque, K. Senecal, H. Curran, C3MechLite: An integrated component library of compact kinetic mechanisms for low-carbon, carbon neutral and zero-carbon fuels, Combust. Flame 282 (2025) 114410.
[19] F. Ghirelli, B. Leckner, Transport equation for the local residence time of a fluid, Chem. Eng. Sci. 59 (3) (2004) 513–523.
[20] L. Berger, A. Attili, M. Gauding, H. Pitsch, Effects of Karlovitz number variations on thermodiffusive instabilities in lean turbulent hydrogen jet flames, Proc. Combust. Inst. 40 (1–4) (2024) 105219.
[21] M.X. Yao, G. Blanquart, Isolating effects of large and small scale turbulence on thermodiffusively unstable premixed hydrogen flames, Combust. Flame 269 (2024) 113657.

[22] H.J. Hussein, S.P. Capp, W.K. George, Velocity measurements in a high-Reynolds-number, momentum-conserving, axisymmetric, turbulent jet, J. Fluid Mech. 258 (1994) 31–75.

[23] B.R. Morton, G.I. Taylor, J.S. Turner, Turbulent gravitational convection from maintained and instantaneous sources, Proc. R. Soc. Lond. Ser. A. Mathematical Phys. Sci. 234 (1196) (1956) 1–23.